Seeing double at Neptune's south pole

S.H. Luszcz-Cook [a,*], I. de Pater [a], M. Ádámkovics [a], H.B. Hammel [b]

[a] *Astronomy Department, University of California, 601 Campbell Hall, Berkeley, CA 94720-3411, USA*
[b] *Space Science Institute, 4750 Walnut Street, Boulder, CO 80301-2532, USA*

ARTICLE INFO

ABSTRACT

Keck near-infrared images of Neptune from UT 26 July 2007 show that the cloud feature typically observed within a few degrees of Neptune's south pole had split into a pair of bright spots. A careful determination of disk center places the cloud centers at $-89.07 \pm 0.06°$ and $-87.84 \pm 0.06°$ planetocentric latitude. If modeled as optically thick, perfectly reflecting layers, we find the pair of features to be constrained to the troposphere, at pressures greater than 0.4 bar. By UT 28 July 2007, images with comparable resolution reveal only a single feature near the south pole. The changing morphology of these circumpolar clouds suggests they may form in a region of strong convection surrounding a neptunian south polar vortex.

1. Introduction

The atmosphere of Neptune is active. In addition to global changes on decadal scales (Lockwood and Jerzykiewicz, 2006; Hammel and Lockwood, 2007), individual clouds evolve on time scales as short as hours (e.g. Limaye and Sromovsky, 1991; Sromovsky et al., 1995, 2001). Near-infrared (NIR) images, which probe Neptune's lower stratosphere and upper troposphere in reflected sunlight, reveal bright bands and cloud features against a dark disk. The pattern of zonal circulation, which is most pronounced at mid latitudes, continues to high southern latitudes, where a bright, unresolved cloud feature is present within a few degrees of the pole. This feature has been seen since the Voyager 2 era (Smith et al., 1989).

Interest in Neptune's global dynamics has been reignited by mid-IR observations of enhanced emission over the south pole relative to the rest of the planet (Hammel et al., 2007; Orton et al., 2007). This enhancement suggests a temperature increase of 4–5 K in the south polar region, and has led these authors to draw parallels with Saturn, where the summer pole is similarly warm in the stratosphere and troposphere (Orton and Yanamandra-Fisher, 2005). Recently it has been observed that both of Saturn's poles exhibit a localized hot spot surrounded by cooler zones, forming circulation cells that make up part of a planet-wide circulation (Fletcher et al., 2008; Dyudina et al., 2008). A global dynamical pattern has also been inferred for Neptune's atmosphere (Martin et al., 2008); it remains to be seen if this pattern includes a polar circulation cell like those on Saturn.

We obtained high spatial resolution NIR images of Neptune's south pole in July 2007, revealing temporal evolution of discrete circumpolar clouds. Here we describe these features, model their properties, and discuss the implications for the dynamics of the neptunian south polar region.

2. Observations and data processing

We observed Neptune from the 10-m W.M. Keck II Telescope on Mauna Kea, Hawaii, on 26–28 July (UT) 2007, as part of a long-term program studying the planet's atmosphere in the NIR. J-, H-, and Kp-band images were taken using the narrow camera of the NIRC2 instrument, coupled to the adaptive optics (AO) system (Table 1). The 1024×1024 array has a pixel size of 9.963 ± 0.011 mas/pixel in this mode (Pravdo et al., 2006), which at the time of observations corresponded to a physical size of $\sim$210 km at disk center.

The data were flat fielded and sky-subtracted, and bad pixels were replaced with the median of the eight surrounding pixels. All images were corrected for the geometric distortion of the array using the 'dewarp' routines provided by P. Brian Cameron,[1] who estimates residual errors at $\lesssim$0.1 pixels. We measured a full width at half maximum (FWHM) of $0.039 \pm 0.005''$ for a stellar point source (SAO 146732) on the days of observation, which is consistent with the diffraction limit of the telescope at 2 µm, and corresponds to an effective resolution of $\sim$800 km at the center of the disk.

The images were photometrically calibrated using the star HD 22686, then converted from units of observed flux density to units of I/F, which is defined as (Hammel et al., 1989):

[1] http://www2.keck.hawaii.edu/inst/nirc2/post_observing/dewarp/nirc2dewarp.pro.

$$\frac{I}{F} = \frac{r^2}{\Omega} \frac{F_N}{F_\odot}$$

where r is Neptune's heliocentric distance, $\pi F_\odot$ is the Sun's flux density at Earth's orbit (Colina et al., 1996), F_N is Neptune's observed

flux density, and Ω is the solid angle subtended by a pixel on the detector. By this definition, $I/F = 1$ for uniformly diffuse scattering from a Lambert surface when viewed at normal incidence.

The 26 July data (Fig. 1) show two distinct features near Neptune's south pole. Other unresolved sources, such as moons and

Table 1
Observations.

Date	Time (UTC)	Filter[a]	Central λ (μm)[a]	Bandpass (μm)[a]	Airmass (")	T_{exp} (s)	N_{exp}
26 July 2007							
Neptune	11:37	J	1.25	0.163	1.21	60	3
Neptune	11:43	Kp	2.12	0.351	1.21	60	3
Neptune	11:49	H	1.63	0.296	1.21	60	5
Neptune	11:58	H	1.63	0.296	1.22	60	5
Neptune	12:07	H	1.63	0.296	1.22	60	5
HD 22686	15:10	J	1.25	0.163	1.33	6	3
HD 22686	15:13	H	1.63	0.296	1.32	6	3
HD 22686	15:15	Kp	2.12	0.351	1.31	10	3
SAO 146732	15:21	Kp	2.12	0.351	1.22	5	3
SAO 146732	15:23	Kp	2.12	0.351	1.22	5	3
SAO 146732	15:24	H	1.63	0.296	1.23	5	3
SAO 146732	15:27	J	1.25	0.163	1.23	5	3
28 July 2007							
Neptune	11:28	H	1.63	0.296	1.21	60	5
Neptune	11:37	H	1.63	0.296	1.21	60	5
Neptune	11:45	H	1.63	0.296	1.22	60	5
SAO 146732	15:20	H	1.63	0.296	1.24	5	3

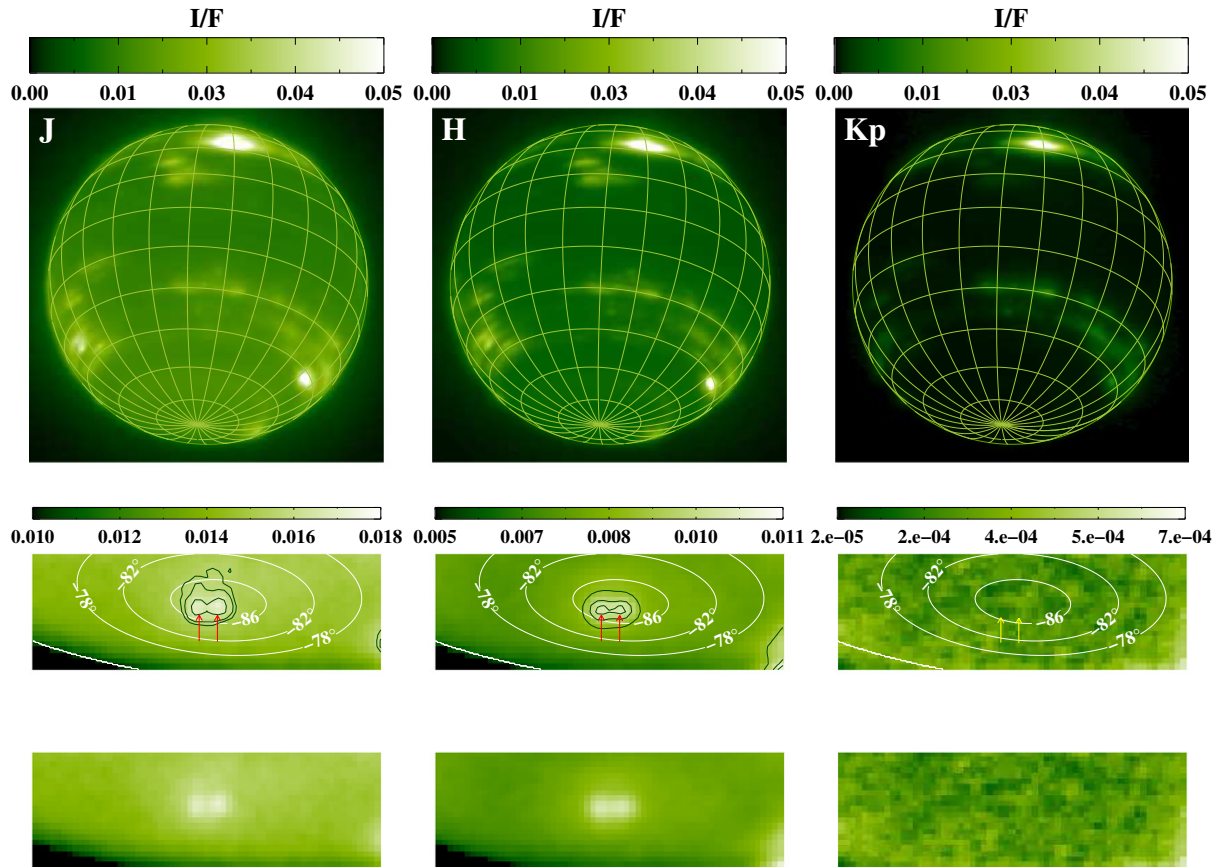[a] http://www2.keck.hawaii.edu/inst/nirc2/.

Fig. 1. J-, H- and Kp-band images from 26 July 2007 in units of *I/F*. The first three images in each filter were averaged together to produce the figure. The top panels all have same color bar. In the top images, the pole is bright due to the convergence of longitude lines; therefore we zoom in on the pole in the bottom panels. The middle row highlights the features by superposing contours at 10%, 20% and 26% above the H-band background; and 3%, 5% and 10% above the J-band background level. Latitude circles at 4° spacings are also shown. The arrows indicate the positions of the two cloud features; in Kp-band the clouds are not above the noise; therefore no intensity contours are plotted. (For interpretation of the references to color in this figure legend, the reader is referred to the web version of this article.)
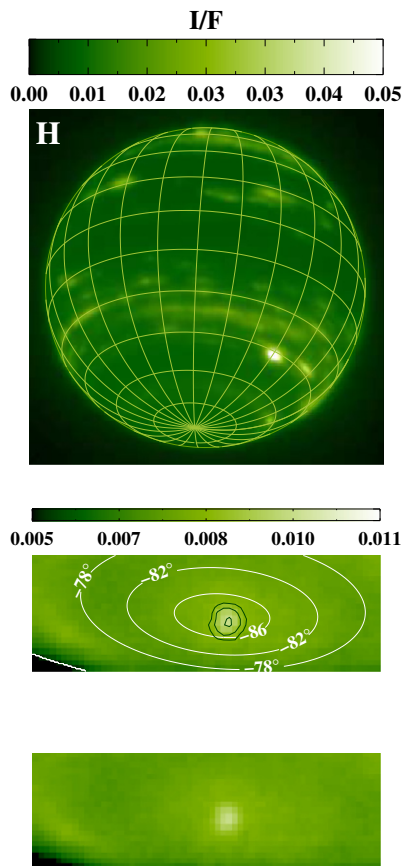
Fig. 2. Average of first three H-band images from 28 July 2007, in units of I/F, with latitude and longitude lines plotted. The middle image highlights the single cloud feature with contours of 5%, 10% and 20% above the background level.

other clouds, do not appear double, so it seems unlikely this is an artifact. The 28 July data (Fig. 2), at comparable resolution, show only a single unresolved polar cloud feature. To determine the total I/F of the unresolved features above the background, we model them as one (for the single cloud on 28 July) or two (for the pair of clouds on 26 July) 2D Gaussians. We use the best-fit parameters from the least-squares fitting routine MPFIT[2] to find the I/F of each cloud feature (Table 2). From experience we estimate the error in the photometry to conservatively be 20%; the errors in the cloud fits are between 4% and 12%. In Kp-band, we do not see the polar cloud features above the noise (Fig. 1). To set an upper limit for the I/F of the clouds in Kp-band, we assume the clouds will be detectible when the mean value of the signal plus noise is equal to one standard deviation above the noise mean. We confirmed this upper limit by convolving the maximum Kp I/F with a Gaussian having the FWHM of the point spread function (PSF) and adding the observed level of noise.

3. Navigation and cloud locations

Neptune's bright and dynamic activity limits the accuracy of image centering when using the planet's limb as a reference, since the PSFs of bright features near the limb often extend off the edge of the disk. To perform the centering more precisely, we found the positions of three of Neptune's moons in each H-band image, and shifted the images in x and y so that the positions of the moons

were best fit to lie on their orbits, as derived from the Planetary Rings Node ephemeris data[3] (Fig. 3). While other methods of aligning images do not necessarily give you the location of disk center, this technique allows us to improve both the relative alignment of the images as well as the determination of disk center coordinates. The centering error in our least-squares fit is on average 0.4 pixels per image, which agrees well with the image-to-image scatter of the positions of individual cloud features. This is an improvement over our centering by limb detection, which we estimate to result in 1–2 pixel errors in the determination of disk center. In J- and K-band we do not have a sufficient number of images to implement our moon centering technique; therefore these images are aligned to the H-band images by eye, to sub-pixel accuracy.

To find the positions of the clouds near the pole, we use the moon-centered H-band images and the solutions from the 2D Gaussian fits (Section 2). We determine the weighted mean location of each cloud in image coordinates, which we then transform into planetocentric latitude and longitude, using the JPL Horizons ephemeris information[4] for sub-observer latitude and longitude at the time of the observations. The errors in the latitude and longitude of the clouds are estimated using a Monte Carlo method, whereby for each parameter involved in calculating the latitude and longitude, a random distribution of values consistent with its probability distribution is generated. These parameters include the array rotation angle (Pravdo et al., 2006), image center coordinates, and cloud center coordinates. For each set of generated parameter values, the latitude and longitude are then calculated; errors are determined as the standard deviations of these simulated data sets.

We find that on 26 July the two cloud features are near, but not directly at the pole as determined by moon orbits: the spot nearest the pole is located at −89.07 ± 0.06° latitude, 293 ± 3° longitude. The second cloud resides approximately 500 km further from the pole, at −87.84 ± 0.06° latitude, 238 ± 2° longitude. The single spot on 28 July is likewise near, but not at, the south pole, at −88.47 ± 0.03° latitude, 86 ± 2° longitude (Table 2).

4. Radiative transfer modeling of features

The J, H, and Kp filters probe various depths through the stratosphere and upper troposphere (Fig. 4); therefore we can use the data to set limits on the heights of the south polar cloud features. To do this, we adapted the radiative transfer (RT) code for Titan from Ádámkovics et al. (2007) for Neptune. We adopt the Neptune temperature profile derived by Lindal (1992) from occultation measurements, and incorporate the major opacity sources that dominate Neptune's 1–5 μm spectrum: we use the H_2 collision-induced absorption coefficients for hydrogen and helium (Borysow et al., 1985, 1988; Borysow, 1991, 1992, 1993), assuming an equilibrium ortho/para ratio for H_2; and the k-distribution coefficients for H_2-broadened methane (Irwin et al., 2006). Following Gibbard et al. (2002), our lower boundary is an optically thick cloud at 3.8 bar, presumably the H_2S cloudtop (de Pater et al., 1991), with a Henyey–Greenstein asymmetry parameter of −0.1. Aerosols are treated as Mie scatterers with real indices of refraction of 1.43 and imaginary indices of refraction n_i = 0. Within a given haze layer, aerosols are characterized by a single particle radius; this radius, along with the altitude range and number density of aerosol particles, is a free parameter, chosen to fit the data. The RT equations are then solved using a two-stream approximation (Toon et al., 1989).

To model the south polar cloud features, we first developed two cloud-free 'background atmosphere' models. For the first model,

[2] Markwardt, C.B., 2008. In: Proc. Astronomical Data Analysis Software and Systems XVIII.

[3] http://pds-rings.seti.org/tools/ephem2_nep.html.
[4] http://ssd.jpl.nasa.gov/horizons.

Table 2
Spot locations and flux densities in units of I/F, as well as the I/F of the region surrounding the clouds. For the clouds, the maximum Kp/J and Kp/H ratios allowed by the data are also given.

Latitude	Longitude	I/F			Max (Kp/J)	Max (Kp/H)
		J	H	Kp		
26 July 2007						
−89.08 ± 0.06°	293 ± 3°	0.039 ± 0.009	0.036 ± 0.008	<0.004	0.11 ± 0.02	0.12 ± 0.02
−87.84 ± 0.06°	238 ± 2°	0.038 ± 0.008	0.033 ± 0.007	<0.004	0.12 ± 0.02	0.13 ± 0.03
Background		0.015 ± 0.003	0.008 ± 0.002	0.00023 ± 0.00006		
28 July 2007						
−88.47 ± 0.03°	86 ± 2°	0.017 ± 0.009	0.042 ± 0.009	<0.005	0.3 ± 0.1	0.12 ± 0.01
Background		0.014 ± 0.003	0.008 ± 0.002	0.00026 ± 0.00009		

we choose the simplest haze distribution consistent with the J-, H-, and K-band I/F values in the region surrounding the polar clouds (Table 3). For comparison, we also find a best model fit to a medium-resolution spectrum from the IRTF Spectral Library (Fig. 5), taken with the SpeX instrument at the NASA Infrared Telescope Facility (IRTF) on Mauna Kea (Rayner et al., 2009). These data are averaged over a significant fraction of Neptune's disk. Although this disk-integrated model has little contribution from the south pole, this second model, which has very different haze properties from the first (Table 3), provides a qualitative test of the sensitivity of our cloud modeling to the choice of model hazes. In addition, fitting to the SpeX data allows us to model the albedo of the deep 'surface' cloud: we find that given our choices of bottom cloud depth and scattering properties, the single-scattering albedo (ω) of the cloud must decrease from 0.55 at 1.1 μm to 0.20 at 1.27 μm and 0.13 at 1.56 μm. These values are reasonably consistent with Roe et al. (2001).

We then model each of the south polar clouds as a perfectly reflecting ($\omega = 1$), optically thick cloud layer with a Mie asymmetry parameter of 0.5. We consider clouds at each of 100 altitudes between 0.4 mbar and 3.8 bar. For each case, we average the resulting 'cloudy' model over H-, J-, and Kp-bands (for comparison with our image data), and subtract the I/F of the 'cloud-free' model to get the I/F contribution from the cloud.

For the 26 July data, we find the ratio of the intensities of the two clouds, which is affected by spot fitting errors but not calibration errors, to be 1.1 ± 0.1 in H-band and 1.0 ± 0.1 in J-band. Therefore, our results are consistent with the clouds being of the same size and at the same altitude. However, since the clouds are unresolved, we do not know the pixel filling fraction for each of the clouds. We can set an upper limit on the clouds' altitudes by comparing the maximum model-derived Kp-to-H and Kp-to-J I/F ratios to the observed values: the higher a cloud is in the atmosphere, the greater the expected Kp-band intensity. The upper limit Kp-to-H and Kp-to-J intensity ratios for each of the clouds, given the uncertainties in H and J, are presented in Table 2. Fig. 6 shows the results of the modeled Kp/H and Kp/J intensities, compared to the maximum of these ratios from the 26 July data.

We find that the upper limit to the altitude of both clouds on 26 July is 0.4 bar. This also provides an estimate on the minimum size of the clouds: if either of the clouds is at 0.4 bar, it must fill at least 10% of a NIRC2 narrow camera pixel to be consistent with the observed H- and J-band intensities. A deeper cloud would necessarily be larger to produce the same values of I/F. For the single cloud on 28 July, we find that its altitude also has an upper limit of 0.4 bar.

The models used in Fig. 6 use the haze distribution that best matches the I/F of the background atmosphere near the cloud features. However, we expect our choice of haze parameters to have little effect on our results. This is because we are interested primarily in the I/F increase due to adding a cloud into the background 'cloud-free' atmosphere. When we ran our second set of models using the simpler haze distribution used to fit the IRTF SpeX data
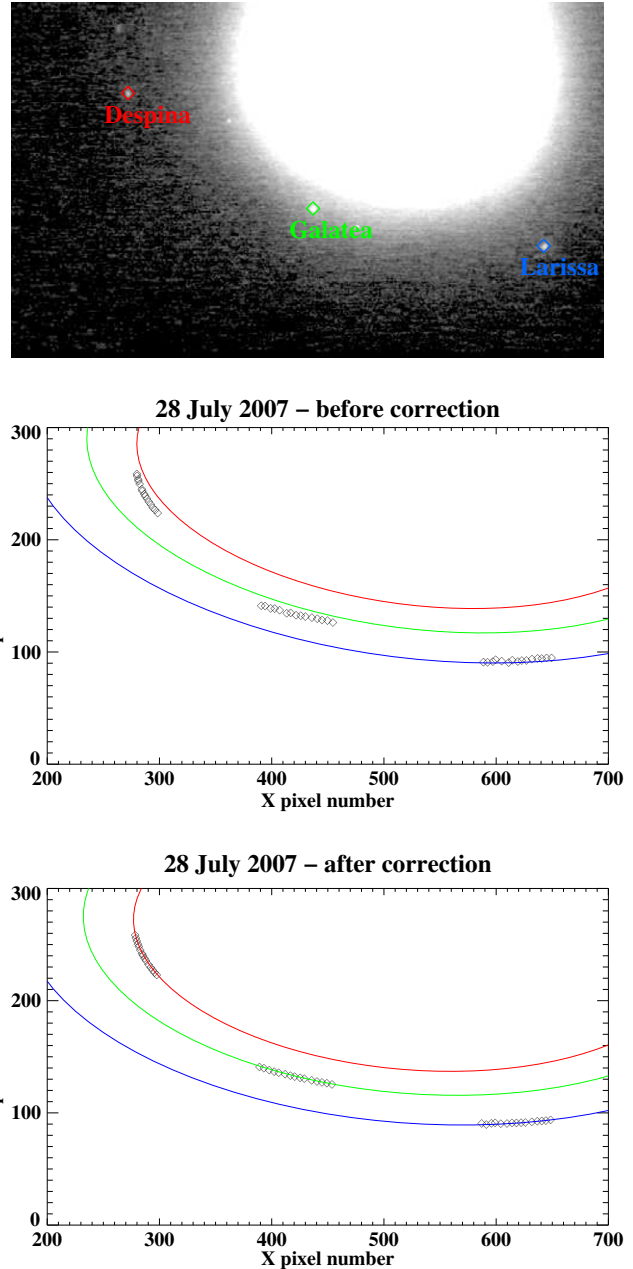

Fig. 3. Fitting disk center using Neptune's moons. The positions of Galatea (green), Larissa (blue) and Despina (red) were found in each image and aligned with the moon orbits to establish the planetary coordinates. The top panel shows the moons in the first H-band image on 28 July. The middle plot shows the orbits relative to the positions of the moons in the images when centered using the planet's limb. The bottom plot shows the moon positions after fitting them to their orbits. (For interpretation of the references to color in this figure legend, the reader is referred to the web version of this article.)
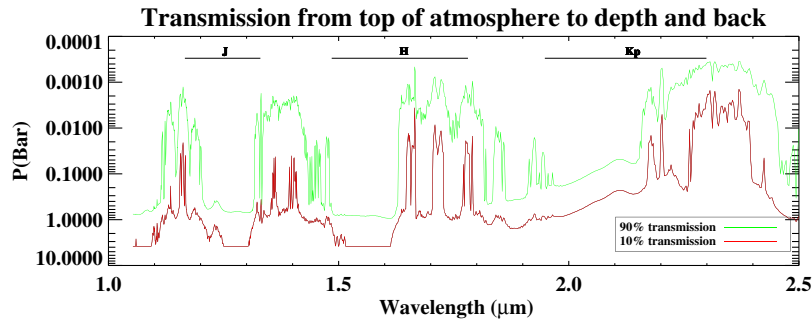
Fig. 4. Two-way transmission in Neptune's atmosphere as predicted by our RT model. The curves show the pressure levels at which 10% (red) and 90% (green) of the light is transmitted to the top of the atmosphere and back. (For interpretation of the references to color in this figure legend, the reader is referred to the web version of this article.)

Table 3
Haze layers, chosen to fit the *I/F* in the three spectral windows in the region around the polar clouds (top); and the IRTF SpeX data (bottom).

P_{min} (mbar)	P_{max} (mbar)	Rad (µm)	n (cm^{-3})
South polar region fit			
5	10	0.8	0.002
45	50	0.2	100
540	1540	0.5	3
SpeX fit			
1.4	20	0.2	12.5
340	1540	2.5	0.07

(Table 2), we found that changing the haze parameters affected the 'cloud-free' and 'cloudy' spectra in a similar way, so that to within 3% the calculated change in *I/F* from a given cloud was independent of the haze parameters.

5. Discussion

A small bright feature at Neptune's south pole has been consistently observed since the Voyager era, implying a stability that contrasts the short (∼hours) lifetime of most small cloud features at lower latitudes (Limaye and Sromovsky, 1991). Our derived upper limit of the altitude of the circumpolar features observed here is consistent with clouds formed by the upwelling and condensation of methane gas, suggesting this may be a region of continuous cloud formation by convection.

The persistence of south polar cloud activity suggests that there is an organized circulation pattern at Neptune's south pole. Such a pattern has been inferred before: Hammel et al. (2007) show that there is a mid-IR temperature enhancement at Neptune's south pole, and Martin et al. (2008) find that the pole is warmer than its surroundings at microwave wavelengths as well. The latter
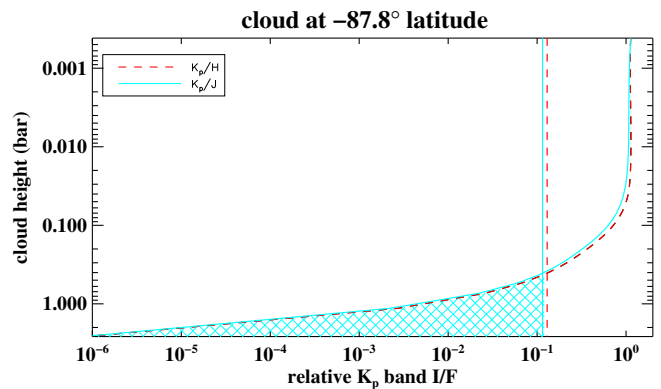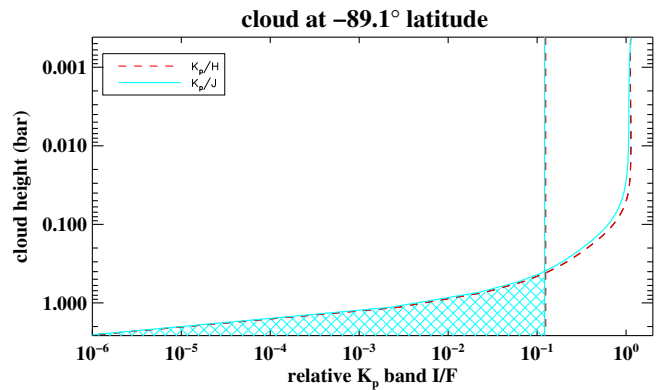

Fig. 6. These plots show the model results for Kp/H intensity ratio (dashed red) and Kp/J ratio (solid cyan) as a function of cloud altitude for each of the two cloud features from 26 July 2007. Dotted lines are at the maximum ratios allowed by the data, showing that the Kp/H ratio sets a stronger limit on the maximum cloud height than the Kp/J ratio. The allowed parameter space is cross-hatched. (For interpretation of the references to color in this figure legend, the reader is referred to the web version of this article.)
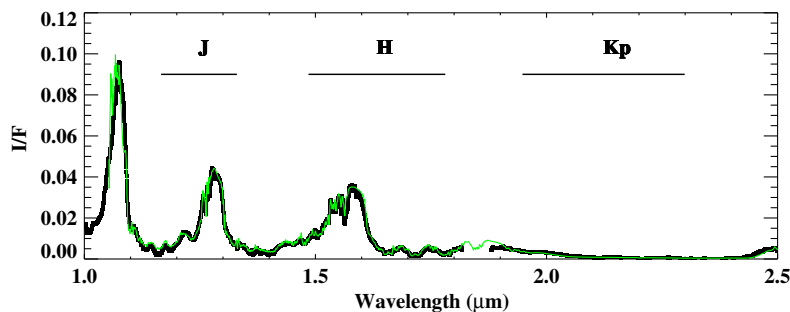

Fig. 5. Comparison of radiative transfer model (green) and long-slit IRTF SpeX spectrum (black). (For interpretation of the references to color in this figure legend, the reader is referred to the web version of this article.)

authors suggest that a global dynamical pattern, in which air near the south pole is subsiding in both the stratosphere and troposphere, can explain the observed high temperatures at both the mid-IR and radio wavelengths. Subsiding motions will adiabatically heat the atmosphere, visible as elevated temperatures in the mid-IR. The subsiding air is likely dry, as condensable gases will condense out during the ascending branch of the dynamical pattern. Such dry conditions enable one to probe much deeper, warmer levels at radio wavelengths, leading to temperature enhancement in microwave observations.

On Saturn, a south polar circulation cell has been observed, in the form of subsidence in a polar vortex surrounded by a region of upwelling (Fletcher et al., 2008). The structure of Saturn's south polar vortex (SPV) (Dyudina et al., 2009) possesses similarities with terrestrial hurricanes, such as a well-formed central eye, concentric eyewalls, and a surrounding ring of strong convection (Fig. 7). The region corresponding to the eye of the SPV is a hot, nearly circular region within a diameter of 4200 km around the south pole. The eye is mostly clear of clouds above ~1 bar (Dyudina et al., 2008), and depleted in phosphine gas (Fletcher et al., 2008), suggesting that this is a region of subsiding air. Surrounding the eye is a ring of discrete, bright clouds in the lower troposphere, which may be analogous to the heavily precipitating clouds encircling the eye of terrestrial hurricanes (Dyudina et al., 2009). The similarity between the temperature enhancement at Neptune's south pole to the enhancement at Saturn's south pole (Hammel et al. (2007) and references therein) first led to the suggestion that Neptune, like Saturn, harbors a long-lived hot south polar vortex (Orton et al., 2007). Our finding that Neptune's south polar cloud feature(s) may be indicative of rigorous convection near, but not at, the pole, supports the analogy between Neptune and Saturn's south polar environments.

The unexpected discovery of a vortex at Saturn's north (winter) pole (Fletcher et al., 2008) implies that polar vortices can exist despite considerable variations in seasonal insolation, and may be general features of giant planet atmospheres. However, possible analogues to Saturn's vortices have yet to be directly observed, as they await the measurement of polar wind speeds by high-inclination space missions. Further details about the morphology of clouds near Saturn's north pole may help us understand the types of cloud morphologies we might expect around polar vortices, and provide insight into how to interpret the behavior of Neptune's polar cloud features in the context of a possible vortex.
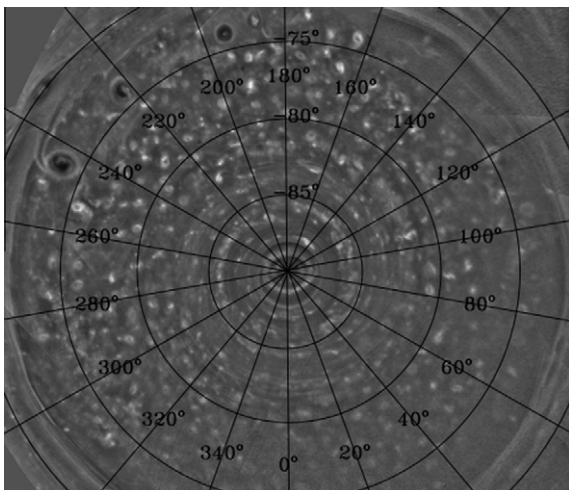

Fig. 7. Map of Saturn's SPV (adapted from Dyudina et al. (2009)) illustrating the small, bright clouds encircling the storm's 'eye', many of which have the same general appearance between 2004 and 2006 observations. Dyudina et al. (2008) conclude these clouds are located in Saturn's lower troposphere.

6. Summary

We have observed a transient double cloud feature near Neptune's south pole on 26 July 2007. The locations of the two features, as determined by the orbits of three of Neptune's moons, suggest they are both circumpolar clouds separated in latitude by ~1.2°. The single circumpolar feature seen on 28 July 2007 is at an intermediate latitude. Radiative transfer modeling indicates that the features on both days are at depths of greater than 0.4 bar, which is consistent with the formation of methane condensation clouds. The morphological change we observe on 26 July, combined with the location of the single cloud on 28 July, may indicate that the bright south polar spot seen since Voyager is not a single stable feature, but rather the signature of persistent cloud activity related to strong convection, perhaps in the region surrounding a polar vortex. Continued high-resolution observations of Neptune's south pole will provide more insight into the dynamics of this region. Such observations should be performed over several hours to capture the evolution of the features. We also await more high-inclination observations of planetary atmospheres to provide further context for understanding giant planet polar environments.

Acknowledgments

References

Ádámkovics, M., Wong, M.H., Laver, C., de Pater, I., 2007. Widespread morning drizzle on Titan. Science 318, 962–965.

Borysow, A., 1991. Modeling of collision-induced infrared absorption spectra of H_2–H_2 pairs in the fundamental band at temperatures from 20 to 300 K. Icarus 92, 273–279.

Borysow, A., 1992. New model of collision-induced infrared absorption spectra of H_2–He pairs in the 2–2.5 micron range at temperatures from 20 to 300 K – An update. Icarus 96, 169–175.

Borysow, A., 1993. Erratum: "Modeling of collision-induced infrared absorption spectra of H_2–H_2 pairs in the fundamental band at temperatures from 20 to 300 K" [Icarus 92(2), 273–279 (Aug 1991)]. Icarus 106, 614.

Borysow, J., Trafton, L., Frommhold, L., Birnbaum, G., 1985. Modeling of pressure-induced far-infrared absorption spectra molecular hydrogen pairs. Astrophys. J. 296, 644–654.

Borysow, J., Frommhold, L., Birnbaum, G., 1988. Collision-induced rototranslational absorption spectra of H_2–He pairs at temperatures from 40 to 3000 K. Astrophys. J. 326, 509–515.

Colina, L., Bohlin, R.C., Castelli, F., 1996. The 0.12–2.5 micron absolute flux distribution of the Sun for comparison with solar analog stars. Astron. J. 112, 307–315.

de Pater, I., Romani, P.N., Atreya, S.K., 1991. Possible microwave absorption by H_2S gas in Uranus' and Neptune's atmospheres. Icarus 91, 220–233.

Dyudina, U.A., and 13 colleagues, 2008. Dynamics of Saturn's south polar vortex. Science 319, 1801.

Dyudina, U.A., and 11 colleagues, 2009. Saturn's south polar vortex compared to other large vortices in the Solar System. Icarus 202, 240–248.

Fletcher, L.N., and 13 colleagues, 2008. Temperature and composition of Saturn's polar hot spots and hexagon. Science 319, 79–81.

Gibbard, S.G., Roe, H., de Pater, I., Macintosh, B., Gavel, D., Max, C.E., Baines, K.H., Ghez, A., 2002. High-resolution infrared imaging of Neptune from the Keck Telescope. Icarus 156, 1–15.

Hammel, H.B., Lockwood, G.W., 2007. Long-term atmospheric variability on Uranus and Neptune. Icarus 186, 291–301.

Hammel, H.B., Baines, K.H., Bergstrahl, J.T., 1989. Vertical aerosol structure of Neptune – Constraints from center-to-limb profiles. Icarus 80, 416–438.

Hammel, H.B., Sitko, M.L., Lynch, D.K., Orton, G.S., Russell, R.W., Geballe, T.R., de Pater, I., 2007. Distribution of ethane and methane emission on Neptune. Astron. J. 134, 637–641.

Irwin, P.G.J., Sromovsky, L.A., Strong, E.K., Sihra, K., Teanby, N.A., Bowles, N., Calcutt, S.B., Remedios, J.J., 2006. Improved near-infrared methane band models and k-distribution parameters from 2000 to 9500 cm^{-1} and implications for interpretation of outer planet spectra. Icarus 181, 309–319.

Limaye, S.S., Sromovsky, L.A., 1991. Winds of Neptune – Voyager observations of cloud motions. J. Geophys. Res. 96, 18941–18960.

Lindal, G.F., 1992. The atmosphere of Neptune – An analysis of radio occultation data acquired with Voyager 2. Astron. J. 103, 967–982.

Lockwood, G.W., Jerzykiewicz, M., 2006. Photometric variability of Uranus and Neptune, 1950–2004. Icarus 180, 442–452.

Martin, S., de Pater, I., Kloosterman, J., Hammel, H.B., 2008. Multi-wavelength observations of Neptune's atmosphere. In: EPSC Abstracts, pp. EPSC2008–A–00277.

Orton, G.S., Yanamandra-Fisher, P.A., 2005. Saturn's temperature field from high-resolution middle-infrared imaging. Science 307, 696–698.

Orton, G.S., Encrenaz, T., Leyrat, C., Puetter, R., Friedson, A.J., 2007. Evidence for methane escape and strong seasonal and dynamical perturbations of Neptune's atmospheric temperatures. Astron. Astrophys. 473, L5–L8.

Pravdo, S.H., Shaklan, S.B., Wiktorowicz, S.J., Kulkarni, S., Lloyd, J.P., Martinache, F., Tuthill, P.G., Ireland, M.J., 2006. Masses of astrometrically discovered and imaged binaries: G78-28AB and GJ 231.1BC. Astrophys. J. 649, 389–398.

Rayner, J.T., Cushing, M.C., Vacca, W.D., 2009. The Infrared Telescope Facility (IRTF) spectral library: Cool stars. ArXiv e-prints.

Roe, H.G., Gavel, D., Max, C., de Pater, I., Gibbard, S., Macintosh, B., Baines, K.H., 2001. Near-infrared observations of Neptune's tropospheric cloud layer with the Lick observatory adaptive optics system. Astron. J. 122, 1636–1643.

Smith, B.A., Soderblom, L.A., Banfield, D., Barnet, C., Beebe, R.F., Bazilevskii, A.T., Bollinger, K., Boyce, J.M., Briggs, G.A., Brahic, A., 1989. Voyager 2 at Neptune – Imaging science results. Science 246, 1422–1449.

Sromovsky, L.A., Limaye, S.S., Fry, P.M., 1995. Clouds and circulation on Neptune: Implications of 1991 HST observations. Icarus 118, 25–38.

Sromovsky, L.A., Fry, P.M., Dowling, T.E., Baines, K.H., Limaye, S.S., 2001. Neptune's atmospheric circulation and cloud morphology: Changes revealed by 1998 HST imaging. Icarus 150, 244–260.

Toon, O.B., McKay, C.P., Ackerman, T.P., Santhanam, K., 1989. Rapid calculation of radiative heating rates and photodissociation rates in inhomogeneous multiple scattering atmospheres. J. Geophys. Res. 94, 16287–16301.